Supplementary Material for

**Experimental evidence that ooid size reflects a dynamic equilibrium between rapid precipitation and abrasion rates**

Elizabeth J. Trower, Michael P. Lamb, and Woodward W. Fischer

Division of Geological and Planetary Sciences, California Institute of Technology, 1200 E California Blvd., Pasadena, CA 91125 USA

This supplementary material document provides an expanded description of the methods used for the model and experiments. This document contains three supporting text subsections (S1 to S4), eleven supporting figures (S1 to S11), and four supporting tables (S1 to S4).

**Text S1. Ooid precipitation rate estimates**

We used three independent sets of data to estimate volumetric ooid precipitation rates to compare with net growth rate constraints from Beaupre et al. (2015), shown in Figure 2. Ferguson et al. (1978) designed a series of experiments in which they grew "proto-ooids" in artificial seawater solutions without current agitation. Although Ferguson et al. (1978) did not specifically provide or calculate a growth rate from these experiments, they stated that they were able, in certain circumstances, to grow synthetic ooids with diameters $\geq$ 400 µm in diameter in timescales of 1-30 days. Taking the longest experimental time (30 days) as a minimum for their experimental rate, a 400 µm "proto-ooid" corresponds to an average precipitation rate of 4.7 x $10^4$ µm$^3$/ooid/hr. Broecker and Takahashi (1966) estimated carbonate precipitation rates from Grand Bahama Bank – they included a number of measurements from two field seasons and a number of locations (n = 16), observing an average rate of 61 mg/cm$^2$/yr, which translates to a volumetric precipitation rate of 6.8 x $10^4$ µm$^3$/ooid/hr for a 200 µm ooid surface or 1.5 x $10^5$ µm$^3$/ooid/hr for a 300 µm ooid surface, both incorporating a specific surface area estimate (see main text). If instead we use a more conservative geometric surface area estimate, these data yield an average ooid precipitation rate of 3.0 x $10^3$ µm$^3$/ooid/hr for a 200 µm ooid surface or 6.7 x $10^3$ µm$^3$/ooid/hr for a 300 µm ooid surface. These geometric surface area estimates can be considered an absolute lower bound for these rates because ooid surfaces are not microscopically smooth (e.g. Figure S1). Finally, we can also use the empirical carbonate precipitation rate equations of Zhong and Mucci (1989) to calculate volumetric ooid precipitation rates. These equations take the general form

$$\log R = \log k + n \log(\Omega_{aragonite} - 1), (1)$$

where $R$ is precipitation rate in µmol/m$^2$/hr, $k$ is a rate constant in µmol/m$^2$/hr, and $n$ is the empirical reaction order. Zhong and Mucci (1989) determined that for aragonite at a salinity of 35 ‰, $\log k \approx 1.11$ and $n \approx 2.26$. For $\Omega_{aragonite}$ = 2–5, this empirical rate equation predicts precipitation rates ranging from 12.9–296 µmol/m$^2$/hr, which translate to volumetric precipitation rates of 1.3 x $10^3$ – 2.9 x $10^4$ µm$^3$/ooid/hr for a 200 µm ooid surface or 2.8 x $10^3$ – 6.5 x $10^4$ µm$^3$/ooid/hr for a 300 µm ooid surface.

**Text S2. Single particle abrasion model**

The single particle abrasion model assumes that particles abrade from impacts with the bed, and thus that the flows are sufficiently dilute such that particle-particle collisions within the flow are negligible (Sklar and Dietrich, 2004). This is a common assumption in sediment transport theory for bed and suspended load transport. Here we modify the total load (bed load and suspension) model (Lamb et al., 2008), which was formulated to find the vertical erosion rate into bedrock from particle impacts, to calculate the volume loss due to abrasion of a given particle of volume $V_p$. We set the volumetric abrasion rate of a given particle that makes successive impacts with the bed to

$$\frac{dV_p}{dt} = V_i I_r \qquad (2)$$

where $V_i$ is the volume eroded per impact, $I_r$ is the number of particle-bed impacts per unit time. The volume eroded per impact is defined as (Sklar and Dietrich, 2004)

$$V_i = \frac{1}{2}\frac{V_p \rho_s w_i^2}{\varepsilon_v} \qquad (3)$$

where $V_p$ is particle volume, $\rho_s$ is particle density (~2.8 g/cm³, see Table S3), $w_i$ is impact velocity normal to the bed, and $\varepsilon_v$ is the kinetic energy per unit volume eroded, which is defined as

$$\varepsilon_v = k_v \frac{\sigma_T^2}{2Y} \qquad (4)$$

where $\sigma_T$ is tensile strength (we chose 1 MPa following Torok, 2007), $Y$ is Young's modulus of elasticity (we chose 20 GPa following Lebedev et al., 2014), and $k_v$ is a dimensionless coefficient that accounts for differences in material properties between the particles and the bed surface (e.g. Scheingross et al., 2014). As in Lamb et al., 2008, the number of impacts per unit time per unit particle area should scale as

$$I_r = \frac{A_2 w_s}{H_{fall}} \qquad (5)$$

where $A_2$ is a dimensionless coefficient, $w_s$ is the gravitational settling velocity, and $H_{fall}$ is typical distance above the bed that a particle is transported. $\frac{H_{fall}}{w_s}$ is the time for a particle to fall to the bed from $H_{fall}$. $A_2 \approx 1/3$ (Sklar and Dietrich, 2004) accounts for the fact that the time between particle-bed impacts depends on the time for a particle to be transported from the bed up to $H_{fall}$, in addition to the time to settle back to the bed. Assuming that $w_s \approx w_i$ (Lamb et al., 2008) and a spherical particle of diameter $D$, Equations (2), (3), (4) and (5) can be combined to calculate the volumetric abrasion rate of a single particle,

$$\frac{dV_p}{dt} = \frac{\pi}{6}\frac{A_2 \rho_s Y w_i^3 D^3}{k_v \sigma_T^2 H_{fall}} \qquad (6)$$

Following Lamb et al. (2008) we calculate $H_{fall}$ by accounting for the vertical concentration profile, $c(z)$, of bedload and suspended sediment using

$$H_{fall} = \frac{1}{c_b}\int_H^{H_b} z\frac{dc}{dz}dz \qquad (7)$$

in which $c_b$ is the near bed concentration, $H$ is the flow depth, $H_b$ is the height of the bedload layer, and $z$ is the height above the bed.

Assuming a Rouse profile for suspended sediment

$$c = c_b\left[\frac{(1-\zeta_z)/\zeta_z}{(1-\zeta_b)/\zeta_b}\right]^P \qquad (8)$$

in which $\zeta_z = z/H$, $\zeta_b = H_b/H$, and $P = \frac{w_s}{\beta \kappa u_*}$ is the Rouse number, $u_*$ is the bed shear velocity, $\kappa = 0.41$ is von Karman's constant, and $\beta$ is a coefficient that relates the diffusivity of sediment to the diffusivity of momentum. Following Sklar and Dietrich (2004), the height of the bed load layer, $H_b$, is calculated as

$$H_b = 1.44D \left(\frac{\tau_*}{\tau_{*c}} - 1\right)^{1/2} \tag{9}$$

where $\tau_* = \frac{u_*^2}{RgD}$ is Shields stress, $g$ is the acceleration due to gravity, $R = \frac{\rho_f - \rho_s}{\rho_f}$ is submerged specific density ($\rho_f$ is fluid density, which was 1.025 g/cm$^3$ for our experiments), and $\tau_{*c} = 0.03$ is critical Shields stress for initial sediment motion.

Particle impact velocity, $w_i$, is calculated as in Lamb et al., 2008 (cf. their eqn. 35):

$$w_{i,\text{eff}} = \left[\int_{-w_s}^{6\sigma_w} (w' + w_s)^3 Pdw'\right]^{1/3} \tag{10}$$

to account for gravitational settling and advection of particles by turbulence, where $\sigma_w$ is the standard deviation of time averaged velocity fluctuations normal to the bed, approximated as $\sigma_w = u_*$ (Lamb et al., 2008) and $P$ is the probability density function of velocity fluctuations ($w'$), defined as

$$P(w') = \frac{1}{\sqrt{2\pi}\sigma_w} e^{-\frac{w'^2}{2\sigma_w^2}} \tag{11}$$

The settling velocity, $w_s$, is assumed to be the terminal settling velocity and calculated using Dietrich (1982):

$$w_s = (RgvW_*)^{1/3} \tag{12}$$

where $v$ is kinematic fluid viscosity (which was 1.3 x 10$^{-6}$ m$^2$/s for our experiments) and $W_*$ is dimensionless settling velocity. $W_*$ is calculated as

$$W_* = R_3 10^{(R_1 + R_2)} \tag{13}$$

$R_1$, $R_2$, and $R_3$ are empirically fitted equations that account for particle size, shape, and density, respectively:

$$R_1 = -3.76715 + 1.92944 \log D_* - 0.09815 (\log D_*)^2 - 0.00575 (\log D_*)^3 + 0.00056(\log D_*)^4 \tag{14}$$

$$R_2 = \left(\log\left(1 - \frac{1-\text{CSF}}{0.85}\right)\right) - (1-\text{CSF})^{2.3} \tanh(\log D_* - 4.6) + 0.3(0.5 - \text{CSF})(1 - \text{CSF})^2 (\log D_* - 4.6) \tag{15}$$

$$R_3 = \left[0.65 - \left(\frac{\text{CSF}}{2.83} \tanh(\log D_* - 4.6)\right)\right]^{(1+\frac{3.5-\text{PS}}{2.5})} \tag{16}$$

where $D_* = \frac{RgD^3}{v^2}$ is dimensionless particle size, CSF is the Corey shape factor (we assume the particles are spherical and use CSF = 1), and PS is the Powers roundness (assuming a spherical particle, we choose PS = 6).

The saltation-abrasion (Sklar and Dietrich, 2004) and total-load (Lamb et al., 2008) bedrock erosion models included a nondimensional constant, $k_v$, that accounts for differences in material properties between particles and bedrock. Experimental constraints on particle abrasion rate as a function of grain size and shear velocity were necessary to determine the appropriate value of $k_v$ for particle abrasion rather than bedrock erosion, which we explicitly determined for ooids. The single particle precipitation-abrasion model fit the experimental data well (Fig. 4a-b) for $k_v = 9$ x 10$^5$ and $\beta = 2$. This value of $k_v$ is similar to the range of values calculated for bedrock erosion ($k_v \sim 10^6$, Sklar and Dietrich, 2004 and Lamb et al., 2008; $k_v \sim 3$ x 10$^5$, Scheingross et al., 2014).

As in the total-load bedrock erosion model (Lamb et al., 2008; Scheingross et al., 2014), the ooid precipitation-abrasion model accounts for viscous damping of particle-bed impacts using a threshold particle Stokes number, $\text{St}_c = \frac{Dw_i\rho_s}{9v\rho_f}$. The threshold required to match key experimental observations (measurable abrasion of medium-sand-sized grains near the threshold of suspension and similarity in magnitude of abrasion rates across a range of $u_*$) (Fig. 4A, Fig. S10) is $\text{St}_c = 9$, lower than that identified for total-load bedrock erosion ($\text{St}_c = 75$;

Scheingross et al., 2014) , but consistent with the critical Stokes number, $St_c \sim 5\text{-}10$, identified as the threshold below which particle deformation during a collision is negligible (Davis et al., 1986; Joseph et al., 2001). The lower Stokes limit might also be due to the roughened bed in the ooid experiments, as compared to a smooth bedrock bed in the experiments of Scheingross et al. (2014).

The model tends to slightly over-predict $|dV_p/dt|$ compared with experimental results, with most trials falling within a factor of three of the model prediction (Fig. S11). This may also indicate additional complexity in the nature of carbonate precipitation that occurred in the experiments not easily captured by the simple precipitation rate equation, particularly with regard to time-dependent changes in surface properties and/or $CO_2$ degassing during active transport (Jacobson and Usdowski, 1975).

**Text S3. Particle size data and estimated abrasion rate**

Abrasion rate is estimated by calculating the change in mean grain volume per unit time using major ($a$), intermediate ($b$), and minor ($c$) axis dimensions determined via Particle Size Analyzer and assuming an ellipsoidal grain shape:

$$\frac{dV_p}{dt} = \frac{\pi(a_f b_f c_f - a_i b_i c_i)}{6t} \tag{17}$$

where $t$ is the length of the experiment. This method of estimation is within an order of magnitude of $dV_p/dt$ estimated by measuring mass loss, while eliminating sources of error associated with attempting to recover 100% of the material from each abrasion mill after each experiment.

Reproducibility of mean particle dimension data is <1% for suitably large samples (>100,000 grains) (Fig. S5). Several experimental trials were run in duplicate or triplicate with the same grain size, propeller speed, carbonate saturation, and duration for each of the three parallel abrasion mills (Table S1). $dV_p/dt$ for individual trials varies by up to an order of magnitude from the mean $dV_p/dt$ for triplicate and this is particularly pronounced for the trials of medium-sand-sized Bahamian ooids at 300 rpm; the remainder of the duplicate/triplicate trials have better reproducibility with $\sigma/|\mu| < 0.5$. This is similar to the variation of experimental bedrock erosion rates (c.f. Table DR1 in Scheingross et al., 2014). Complexities relating to carbonate chemistry may also contribute to variations between trials. For example, differences in surface properties between the abrasion mill walls and the propellers could affect the quantity of carbonate precipitated on these surfaces during each trial, which in turn would affect $\Omega_{aragonite}$ and $(dV_p/dt)_{abrasion}$.

**Text S4. Ooid lifetimes and equilibrium timescales**

Radiocarbon dating of modern marine ooids suggests that typical ooid lifetimes ($\tau_{ooid}$) are $\leq 2000$ yr (Beaupré et al., 2015; Duguid et al., 2010), so this is a relevant timescale to compare with the predicted time to reach an equilibrium size ($t_{eq}$). For this exercise, we assume a spherical cortex with a diameter of 50 μm and calculate the expected time for this nucleus to reach a diameter of 500 μm, chosen both because this is a common ooid size in modern environments and the rock record (and therefore a likely possible choice for $D_{eq}$ in typical ooid-forming environments) and because $D_{eq}$ of this size can be achieved using many reasonable parameter combinations (Fig. 5b). Although we use a constant radial growth rate in the abrasion-precipitation model detailed in the main manuscript, here we apply a constant volume rate to simplify the calculation as we are looking for order of magnitude comparisons. Net growth rate constraints from Beaupré et al. (2015) correspond with growth times ranging

4

from ~1300 yr at their most rapid growth rate to ~23,000 yr at their slowest growth rate. These rates are therefore similar to or much longer than $\tau_{ooid}$, which would suggest that many ooids do not reach an equilibrium size within their lifetime. Constraints on carbonate precipitation rate from other data sets (Fig. 2) tell a different story: at the slowest rate, growth time is calculated to be ~6 yr, while at the most rapid growth rate, growth time is ~400 hr. These timescales are much shorter than $\tau_{ooid}$, implying that, if these rates are correct, ooids likely approach $D_{eq}$ very rapidly relative to their overall lifetime. The rapid precipitation and abrasion rates from our experiments support this latter conclusion and therefore emphasize the importance of dynamic equilibrium in ooid growth.
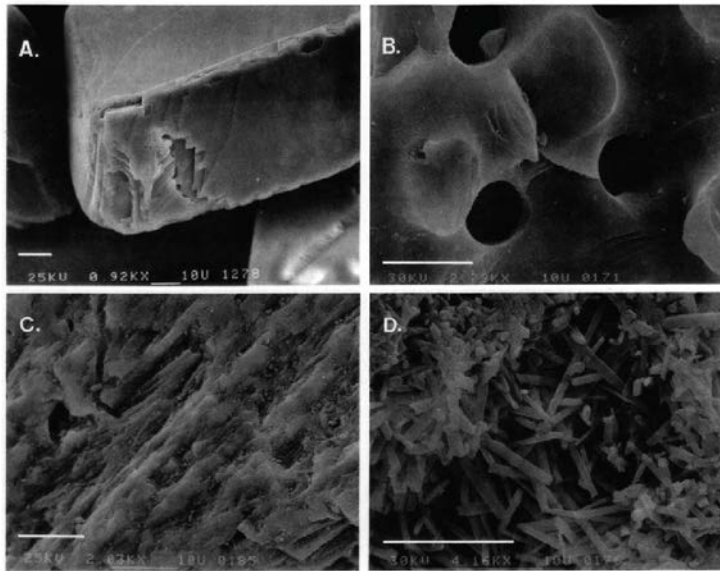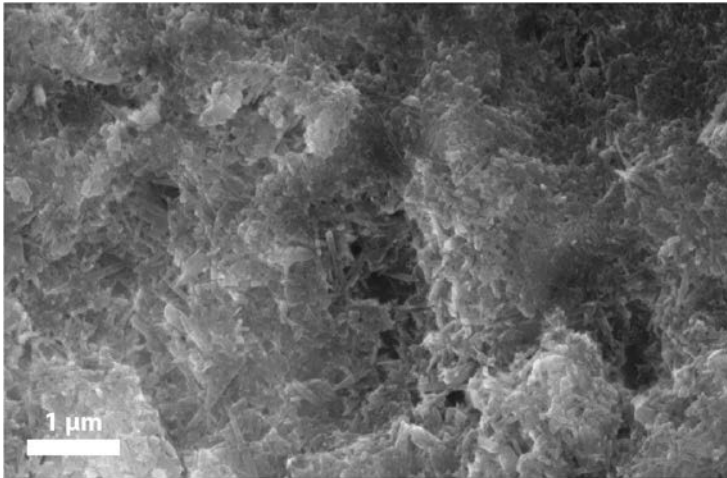
**Figure S1.** SEM image of un-abraded ooid surface area, showing texture comparable to coral fragment surfaces from Walter and Morse (1984), reproduced in lower four panels (scale bars in Walter and Morse SEM images are 10 microns). Ooid surface area is most comparable to panel C.
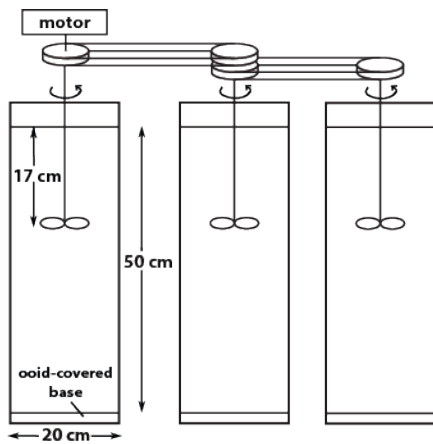
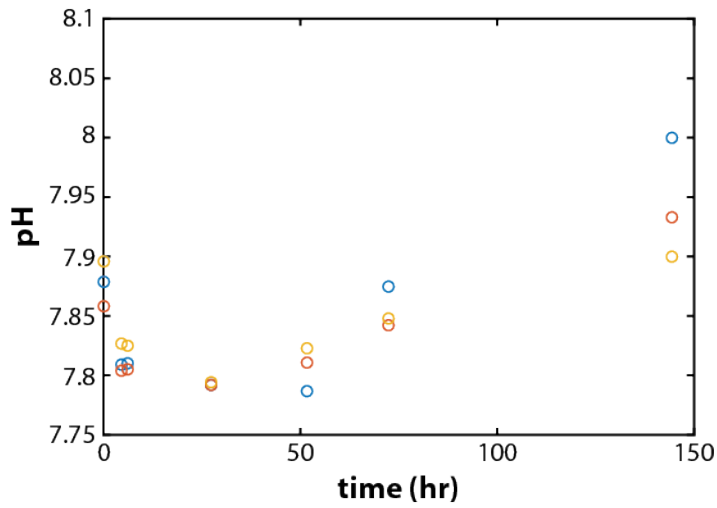**Figure S2.** Schematic of experimental setup.



**Figure S3.** Example of pH data over the duration of an experiment. This experiment was run with medium-sand Bahamian ooids at 350 rpm ($u_* = 0.048$ m/s) and resulted in net abrasion of ooids (see Table S1). Each color corresponds to one of the three abrasion mills that were run in parallel (see Figure S2).
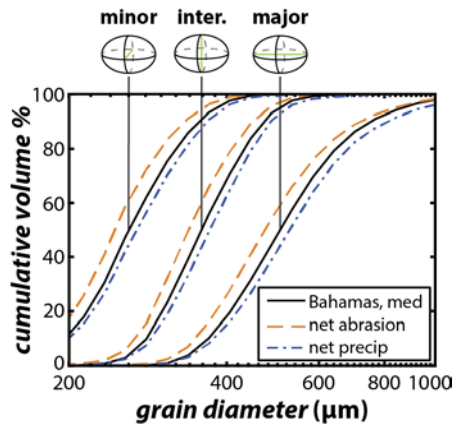
**Figure S4.** Cumulative distribution curves of major, intermediate, and minor axis dimensions of ooids determined via Particle Size Analyzer. Medium-sand-sized Bahamian ooid populations are shown prior to (solid black lines) and after an abrasion experiment (dashed orange lines) and a precipitation experiment (dot dash blue lines).
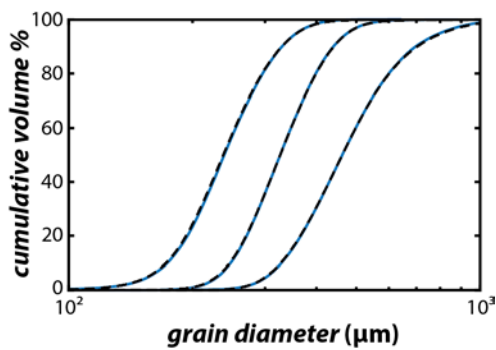


**Figure S5.** Replicate analyses of major, intermediate, and minor axis dimensions of unabraded medium-sand-sized Bahamian ooids. Blue and dashed black lines are cumulative distribution curves for replicate analyses.
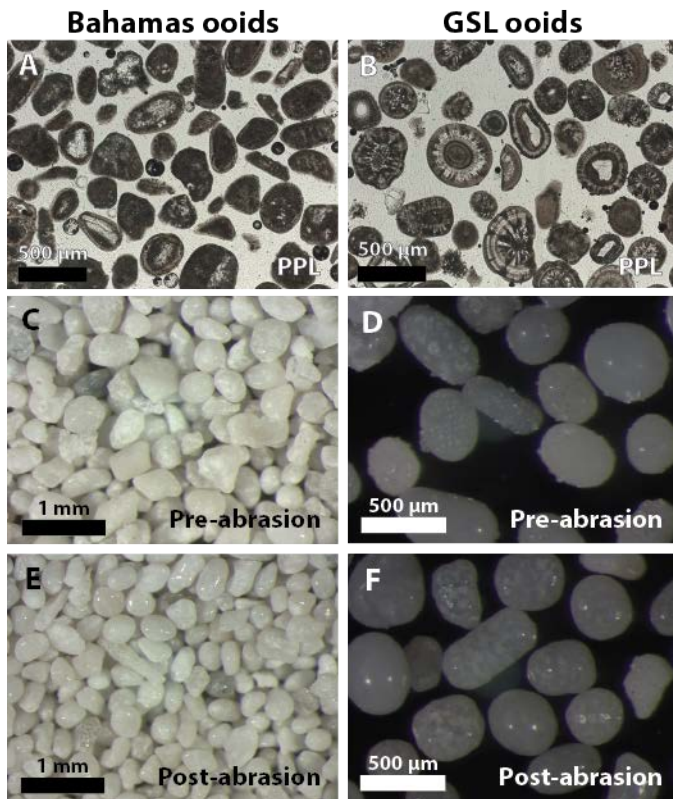
**Figure S6.** Microscopy of Bahamian (A, C, E) and GSL ooids (B, D, F) used for experiments. (A-B) Photomicrograph of thin sections of sieved medium-sand-sized ooids. (C-F) Surface textures of ooids prior to (C-D) and after (E-F) an abrasion experiment.
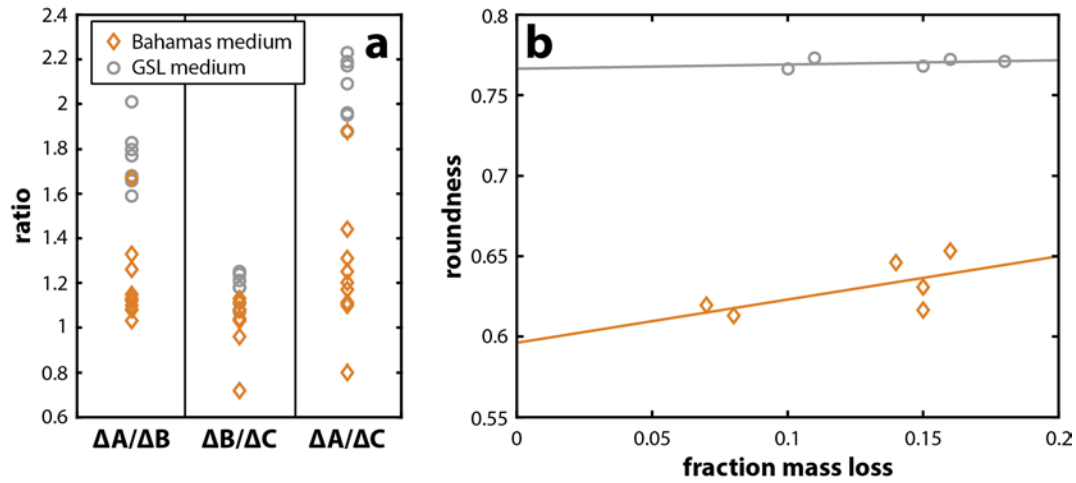
**Figure S7.** Shape characteristics of medium-sand-sized Bahamian and GSL ooids, (a) comparing the ratios of change in major (ΔA), intermediate (ΔB), and minor (ΔC) axis dimensions. Notably, the major axis dimensions of GSL ooids are decreased by ~2 times the intermediate or minor axis dimensions, a pattern that is not present in the Bahamian ooids. (b) Bahamian ooids display a trend of increasing roundness with increasing mass loss, which is not observed in GSL ooids, which are significantly more round prior to experimentation. We use Wadell roundness, which is calculated as

$$Roundness = \frac{\sum_{i=1}^{n} \frac{r_i}{R}}{n}$$

where $r_i$ are the radii of curvature of particle corners, $R$ is the radius of the largest inscribed circle, and $n$ is the number of particle corners measured.
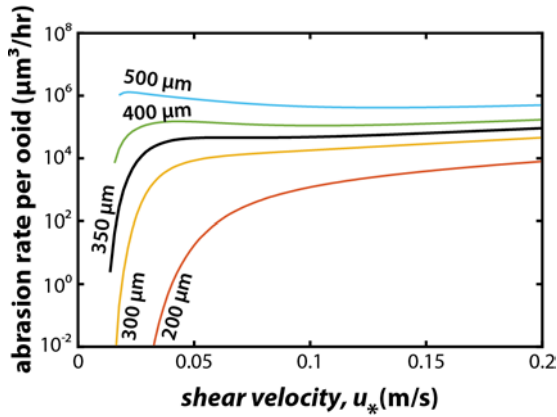
**Figure S8.** Modeled abrasion rate ($-dV_p/dt$) as a function of shear velocity ($u_*$) for a range of grain size ($D$), illustrating the subtle local minimum in abrasion rate predicted for $D > 350$ μm.
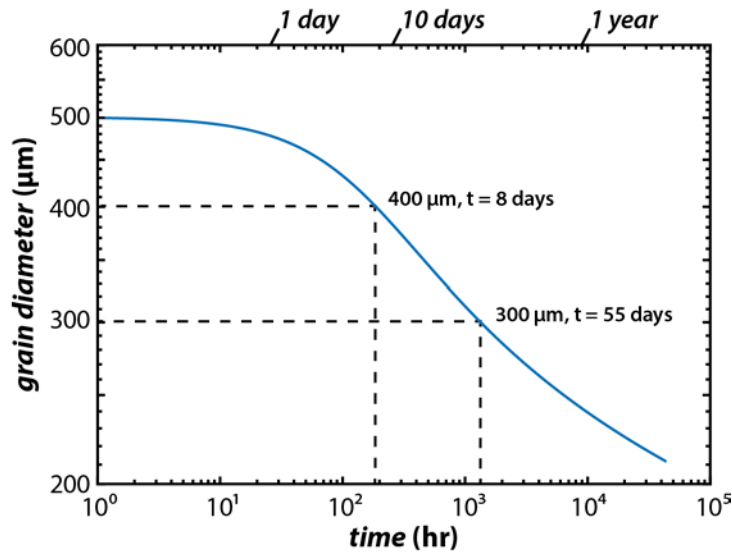


**Figure S9.** Predicted decay in ooid size over time using calibrated abrasion model. In this model we turn precipitation off by setting $\Omega_{aragonite} = 1$ and choose $u_* = 0.05$ m/s, which translates to mixed bedload and suspended load transport for 500 μm ooids. Without being balanced by precipitation, abrasion is predicted to be rapid, with initial 500 μm ooids decreasing to 400 μm in about 8 days of movement and 300 μm in 55 days. The stability of ooids > 300 μm in size in high energy shoal environments is therefore difficult to explain without the balance of precipitation while grains are in motion.
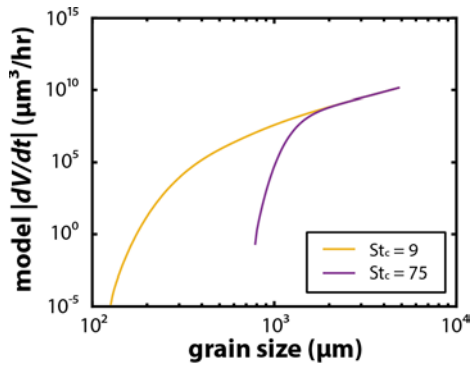
**Figure S10.** Modeled abrasion rate ($-dV_p/dt$) as a function of grain size (D) for $u_* = 0.05$ m/s for the Stokes threshold ($St_c = 9$) that matches experimental data and for the Stokes threshold ($St_c = 75$) for bedrock erosion from Scheingross et al., 2014.
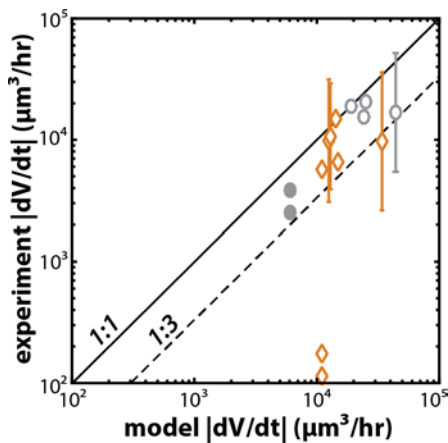


**Figure S11.** Comparison of experimental $|dV/dt|$ vs. model predictions for $|dV/dt|$, using the same symbols as in Fig. 4. Data from the medium-sand-sized Bahamian experiments at 250 rpm (Table S1) cannot be plotted here because the model predicts net abrasion for these conditions, but the experiments yielded net precipitation. The fit for these data and the other trials that fall far below the 1:1 line can be improved by increasing the Stokes threshold toward $St_c \sim 13$ (see Fig. 4b), suggesting that, although $St_c \sim 9$ is the best fit for most data, it does not quite capture the onset of viscous damping effects for these combinations of grain size and shear velocity. Data from the fine-sand-sized Bahamian experiment (Table S1) are also not plotted here because the experimental rates are more than two orders of magnitude slower than model predictions (see Fig. 4b), perhaps indicating a kinetic limitation to precipitation for this combination of experimental conditions.

| Grain type | Grain diameter (μm) | Propeller speed (rpm) | Shear velocity (m/s)[b] | $\Omega_{aragonite}$ | Time (hr) | n | Geometric mean $dV_p/dt$ (μm³/hr) | Geom. std. dev. |
|---|---|---|---|---|---|---|---|---|
| _Experiment set 1 – constant grain size_ | | | | | | | | |
| Bahamas medium | 334 | 250 | 0.044 | 2.9 | 216.5 | 3 | $7.8 \times 10^3$ | 1.5 |
| | | 300 | 0.048 | | 187.5 | 3 | $-4.8 \times 10^2$ | 8.7 |
| | | 350 | 0.052 | | 336.6 | 3 | $-9.8 \times 10^3$ | 1.3 |
| | | 400 | 0.057 | | 220 | 1 | $-1.5 \times 10^4$ | |
| | | 450 | 0.062 | | 171.1 | 1 | $-6.4 \times 10^3$ | |
| | | 500[a] | 0.068 | | 257 | 2 | $-1.1 \times 10^4$ | 1.0 |
| | | 1000 | 0.15 | | 373.2 | 3 | $-9.9 \times 10^3$ | 1.2 |
| GSL medium | 346 | 250[a] | 0.044 | 2.9 | 213.9 | 1 | $-1.9 \times 10^4$ | |
| | | 400[a] | 0.057 | | 214.3 | 1 | $-1.5 \times 10^4$ | |
| | | 450 | 0.062 | | 171.1 | 1 | $-2.1 \times 10^4$ | |
| | | 1000 | 0.15 | | 358.9 | 3 | $-1.7 \times 10^4$ | 1.1 |
| _Experiment set 2 – varying grain size_ | | | | | | | | |
| Bahamas fine | 204 | 500 | 0.068 | 2.9 | 257 | 1 | 51 | |
| Bahamas medium | 334[a] | | | | 257 | 2 | $-1.1 \times 10^4$ | 1.0 |
| GSL fine | 207 | 250 | 0.044 | 2.9 | 213.9 | 1 | $3.8 \times 10^3$ | |
| GSL medium | 346[a] | | | | | 1 | $-1.9 \times 10^4$ | |
| GSL fine | 207 | 400 | 0.057 | 2.9 | 214.3 | 1 | $2.5 \times 10^3$ | |

| GSL medium | 346[a] | | | | | 1 | -1.5 x 10$^4$ | |
|---|---|---|---|---|---|---|---|---|

**Table S1.** Abrasion mill experiment parameters.

[a]These trials are included in both experiment sets.
[b]Shear velocities were estimated following Sklar and Dietrich (2001) and Scheingross et al. (2014) and using observations of thresholds of motion and suspension to interpolate between propeller speed settings.

|  | Instant Ocean[a] | Open ocean[a] | Caribbean[b] | Great Salt Lake[cd] |
|---|---|---|---|---|
| Salinity (permil) | 29.65 | 35 | 38.6 | 148 |
| *Major cations and anions (mM)* | | | | |
| $Na^+$ (mM) | 462 | 470 | 516 | 2043 |
| $K^+$ | 9.4 | 10.2 | 11.0 | 71.6 |
| $Mg^{2+}$ | 52 | 53 | 59 | 167 |
| $Ca^{2+}$ | 9.4 | 10.3 | 11.5 | 5.5 |
| $Cl^-$ | 521 | 550 | 603 | 2372 |
| $SO_4^-$ | 23 | 28 | 31 | 96 |
| pH | 8.21 | 8.18 | | 8.2 |
| $TCO_2$ | 1.99 | 1.94 | | 5.36 |
| *Carbonate speciation (mM), calculated at pH 8 and 22°C[e]* | | | | |
| $CO_2$ | 0.011 | 0.011 | | 0.0021[f] |
| $HCO_3^-$ | 1.82 | 1.75 | | 0.53[f] |
| $CO_3^{2-}$ | 0.16 | 0.18 | | 4.83[f] |
| $\Omega_{aragonite}$ | 2.95 | 2.93 | | 3.61[f] |

**Table S2.** Composition of Instant Ocean artificial seawater compared with fluid compositions typical of some key ooid-forming environments.

[a]Salinity, major cation/anion, pH, and $TCO_2$ data from *Atkinson and Bingman* [1997].

[b]Salinity and major cation/anion data from Baseggio (1974).

[c]Salinity and major cation/anion data from Rupke and McDonald (2012).

[d]pH and $TCO_2$ data from Anderson et al. (2013).

[e]Carbonate speciation calculated using $pK_1$ and $pK_2$ using the empirical equations from Prieto and Millero (2002).

[f]Carbonate speciation calculated using $pK_1$, $pK_2$, and $pK_{sp}$ for Dead Sea brines of similar salinity from Sass and Ben-Yaakov (1977).

| Ooid type | Density (g/cm³, ± 2%) |
|---|---|
| Bahamas, medium | 2.76 |
| GSL, medium | 2.84 |

**Table S3.** Measured densities of un-abraded medium-sand-sized Bahamas and GSL ooids.

| Ooid type | A (mean major axis dimension, μm) | B (mean intermediate axis dimension, μm) | C (mean minor axis dimension, μm) | Aspect ratio (A/C) |
|---|---|---|---|---|
| Bahamas, medium | 481 | 334 | 244 | 1.97 |
| GSL, medium | 476 | 346 | 276 | 1.72 |

**Table S4.** Dimensions of un-abraded medium-sand-sized Bahamas and GSL ooids.

**References**

Anderson, R., Bird, J., Meneske, M., Stefurak, E., Berelson, W., Petryshyn, V., Shapiro, R., Sessions, A., Tripati, A., Corsetti, F., 2013. Ooid formation in the Great Salt Lake, Utah: Insights from clumped isotope paleothermometry. AGU Fall Meeting Abstracts 1, 1941.

Atkinson, M., Bingman, C., 1997. Elemental composition of commercial seasalts. J. Aquaric. Aquat. Sci 8, 39-43.

Baseggio, G., 1974. The composition of sea water and its concentrates, Fourth Symposium on Salt, pp. 351-358.

Beaupré, S.R., Roberts, M.L., Burton, J.R., Summons, R.E., 2015. Rapid, high-resolution ^{14}C chronology of ooids. Geochimica et Cosmochimica Acta 159, 126-138.

Broecker, W.S., Takahashi, T., 1966. Calcium carbonate precipitation on the Bahama Banks. Journal of Geophysical Research 71, 1575-1602.

Davis, R.H., Serayssol, J.-M., Hinch, E., 1986. The elastohydrodynamic collision of two spheres. Journal of Fluid Mechanics 163, 479-497.

Dietrich, W.E., 1982. Settling velocity of natural particles. Water resources research 18, 1615-1626.

Duguid, S.M.A., Kyser, T.K., James, N.P., Rankey, E.C., 2010. Microbes and Ooids. Journal of Sedimentary Research 80, 236-251.

Ferguson, J., Bubela, B., Davies, P.J., 1978. Synthesis and possible mechanism of formation of radial carbonate ooids. Chemical Geology 22, 285-305.

Jacobson, R.L., Usdowski, E., 1975. Geochemical controls on a calcite precipitating spring. Contributions to Mineralogy and Petrology 51, 65-74.

Joseph, G., Zenit, R., Hunt, M., Rosenwinkel, A., 2001. Particle–wall collisions in a viscous fluid. Journal of Fluid Mechanics 433, 329-346.

Lamb, M.P., Dietrich, W.E., Sklar, L.S., 2008. A model for fluvial bedrock incision by impacting suspended and bed load sediment. Journal of Geophysical Research: Earth Surface (2003–2012) 113.

Lebedev, M., Wilson, M.E., Mikhaltsevitch, V., 2014. An experimental study of solid matrix weakening in water-saturated Savonnières limestone. Geophysical Prospecting 62, 1253-1265.

Prieto, F.J.M., Millero, F.J., 2002. The values of pK 1+ pK 2 for the dissociation of carbonic acid in seawater. Geochimica et Cosmochimica Acta 66, 2529-2540.

Rupke, A.L., McDonald, A., 2012. Great Salt Lake Brine Chemistry Database, 1966-2011. Utah Geological Survey.

Sass, E., Ben-Yaakov, S., 1977. The carbonate system in hypersaline solutions: Dead Sea brines. Marine Chemistry 5, 183-199.

Scheingross, J.S., Brun, F., Lo, D.Y., Omerdin, K., Lamb, M.P., 2014. Experimental evidence for fluvial bedrock incision by suspended and bedload sediment. Geology 42, 523-526.

Sklar, L.S., Dietrich, W.E., 2004. A mechanistic model for river incision into bedrock by saltating bed load. Water Resources Research 40.

Török, Á., 2007. Influence of fabric on the physical properties of limestones. Fracture and Failure of Natural Building Stones: Applications in the Restoration of Ancient Monuments, 487.

Walter, L.M., Morse, J.W., 1984. Reactive surface area of skeletal carbonates during dissolution: effect of grain size. Journal of Sedimentary Research 54.

Zhong, S., Mucci, A., 1989. Calcite and aragonite precipitation from seawater solutions of various salinities: Precipitation rates and overgrowth compositions. Chemical Geology 78, 283-299.